Meniscus Oscillations Driven by Flow Focusing Lead to Bubble Pinch-Off and Entrainment in a Piezoacoustic Inkjet Nozzle

Arjan Fraters,[1] Maaike Rump,[1] Roger Jeurissen,[2] Marc van den Berg,[3] Youri de Loore,[3] Hans Reinten,[3] Herman Wijshoff,[3,4] Devaraj van der Meer,[1] Detlef Lohse,[1] Michel Versluis,[1] and Tim Segers[5,1,*]

[1] *Physics of Fluids group, Max-Planck Center Twente for Complex Fluid Dynamics, Department of Science and Technology, MESA+ Institute, and J. M. Burgers Centre for Fluid Dynamics, University of Twente, 7522 NB Enschede, Netherlands*

[2] *Department of Applied Physics, Eindhoven University of Technology, 5600 MB Eindhoven, Netherlands*

[3] *Canon Production Printing Netherlands B.V., 5914 HH Venlo, Netherlands*

[4] *Department of Mechanical Engineering, Eindhoven University of Technology, 5600 MB Eindhoven, Netherlands*

[5] *BIOS Lab-on-a-Chip group, Max-Planck Center Twente for Complex Fluid Dynamics, MESA+ Institute for Nanotechnology, University of Twente, 7522 NH Enschede, Netherlands*

(Received 3 May 2021; revised 13 July 2021; accepted 1 October 2021; published 27 October 2021; corrected 11 November 2021)

The stability of high-end piezoacoustic drop-on-demand (DOD) inkjet printing is sometimes compromised by the entrainment of an air bubble inside the ink channel. Here, bubble pinch-off from an oscillating meniscus is studied in an optically transparent DOD printhead as a function of the driving waveform. We show that bubble pinch-off follows from low-amplitude high-frequency meniscus oscillations on top of the global high-amplitude low-frequency meniscus motion that drives droplet formation. In a certain window of control parameters, phase inversion between the low- and high-frequency components leads to the enclosure of an air cavity and bubble pinch-off. Although phenomenologically similar, bubble pinch-off is not a result of capillary-wave interaction such as observed in drop impact on a liquid pool. Instead, we reveal geometrical-flow focusing as the mechanism through which, at first, an outward jet is formed on the retracted concave meniscus. The subsequent high-frequency velocity oscillation acts on the now toroidal-shaped meniscus and it accelerates the toroidal ring outward, resulting in the formation of an air cavity that can pinch off. Through incompressible boundary-integral simulations, we reveal that bubble pinch-off requires an unbalance between the capillary and inertial time scales and that it does not require acoustics. The critical control parameters for pinch-off are the pulse timing and amplitude. To cure the bubble entrainment problem, the threshold for bubble pinch-off can be increased by suppressing the high-frequency driving through appropriate waveform design. The present work therefore aids the improvement of the stability of inkjet printers through a physical understanding of meniscus instabilities.

DOI: 10.1103/PhysRevApplied.16.044052

I. INTRODUCTION

Piezo-inkjet printing is an accurate and contactless method to deposit ink droplets on a substrate [1–4]. Droplets are formed on demand from a nozzle by actuating a piezoelectric element. The piezo deforms the channel wall upon electrical stimulation, resulting in acoustic pressure waves that jet the ink out of the nozzle [5]. Piezo-inkjet printing is used in high-end industrial printers for on-demand personalized printing of documents, graphic art, and packaging, the main reason being its high reliability, high print quality, and its compatibility with a wide range of inks. The aforementioned properties also make piezo-inkjet printing an excellent technique for several emerging additive manufacturing applications, such as printing electronics [6–14], pharmaceutics [15], biomaterials [16–19], and even the lubrication of ball bearings [20].

Although piezo-inkjet printing is a highly reliable droplet deposition technique, the droplet-formation process is sometimes compromised by the entrainment of an air bubble [21–30]. The entrained air bubble disturbs or even stops the jetting process and thereby dramatically reduces the printing quality and reliability. Previously, several mechanisms have been identified by which bubbles can be entrained in the ink channel. First, on the nozzle plate at the nozzle exit, dirt particles or an ink layer can trigger bubble entrainment by disturbing the jetting process at the nozzle exit [21]. Second, a dirt particle

*t.j.segers@utwente.nl

in the ink can trigger bubble nucleation upon its interaction with the oscillating meniscus interface and, third, a bubble can nucleate on the particle through cavitation inception in the rarefaction pressure wave [30]. However, bubbles can also be entrained in the absence of dirt particles or an ink layer, i.e., by yet another physical mechanism. Figure 1 shows back-illuminated [32,33] images of such a bubble pinch-off and entrainment event that is observed in a squeeze-type piezo-inkjet printhead with a 70-μm-diameter optically transparent nozzle exit (Microdrop Technologies GmbH, Autodrop Pipette AD-K-501), driven by a rectangular push-pull pulse (amplitude 150 V, width 30 μs). First, a droplet is ejected and, subsequently, the meniscus retracts back into the nozzle and a bubble pinches off when the meniscus motion reverses from its inward motion to an outward motion, away from the ink channel. Note that the ink appears transparent inside the glass nozzle and dark outside—oppositely to air—due to the similar refractive indices of ink and glass and their mismatch with that of air. The bubble pinch-off event is shown in more detail in Fig. 1(b). The figure shows that the central region of the meniscus moves inward while the outer region of the meniscus moves outward. As a result, an air cavity forms that eventually closes, thereby pinching off an air bubble.

Bubble pinch-off as shown in Fig. 1 is found to occur only within certain windows of the piezo driving conditions. This is illustrated in Fig. 2, where two examples of a bubble pinch-off window are given for a rectangular pull-push pulse with amplitude A and width Δt [Fig. 2(a)]. In the first example in Fig. 2(b), the pulse amplitude A is varied with all other parameters fixed ($\Delta t = 30$ μ s). Note from the retracted meniscus amplitude that the injected momentum increases linearly with the pulse amplitude, as expected [34]. A window of bubble pinch-off is observed between pulse amplitudes of 140 V and 150 V. Given the nature of meniscus instabilities, meaning that the growth time shortens and the oscillation amplitude increases with increasing acceleration [35–37], it is expected that bubble pinch-off will always occur above a certain threshold amplitude. Surprisingly, no bubble pinch-off is observed at amplitudes larger than 160 V. In the second example [see Fig. 2(c)], the pulse width is varied. Bubble pinch-off is observed between pulse widths of 70 μs and 75 μs. The bubble size initially increases and then decreases, with a maximum radius between 72 μs and 73 μs.

An oscillating meniscus can be destabilized by several mechanisms, including the classical Rayleigh-Taylor instability [35,36,38] and the parametrically driven meniscus instability [37,39]. A Rayleigh-Taylor instability grows on a flat interface between two fluids with different density, i.e., in this particular case, the ink and air. The two fluids are accelerated at a rate high enough for the inertial forces to overcome the restoring surface tension. The parametrically driven meniscus instability grows on an initially flat meniscus at the subharmonic of the frequency at which the meniscus is driven (period doubling). The meniscus can also be destabilized at an intermediate Ohnesorge number by an inhomogeneous velocity field at the meniscus, due to the finite transport time of viscous-drag-induced vorticity

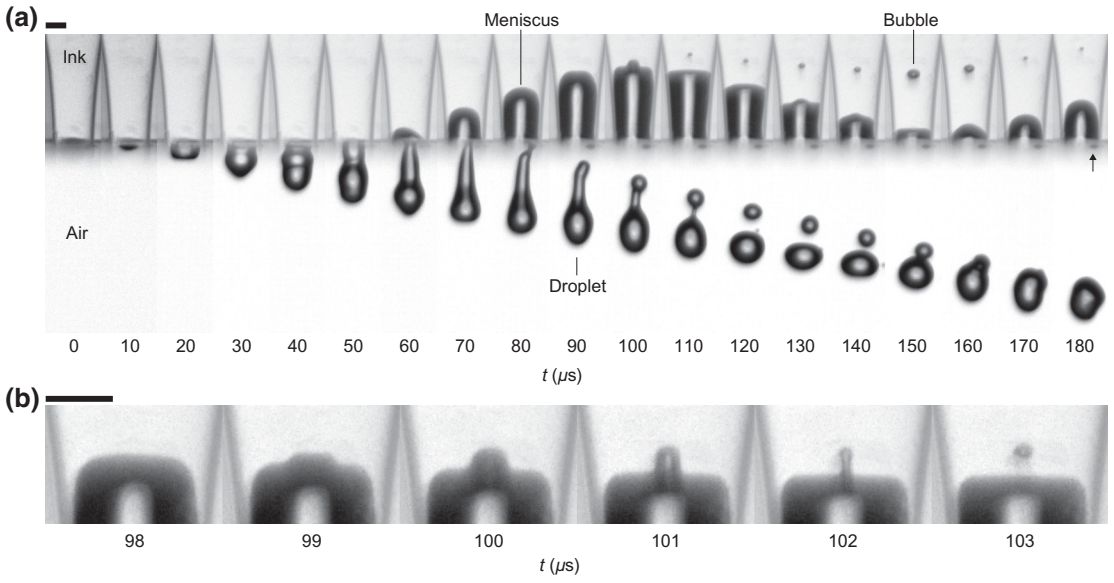

FIG. 1. (a) Bubble pinch-off and entrainment in a 70-μm-diameter nozzle of a piezo drop-on-demand inkjet printhead. The piezo actuation pulse is a rectangular push-pull pulse with a 150-V amplitude and a 30-μs width. The images are recorded using 8-ns single-flash stroboscopic imaging with illumination by laser-induced fluorescence (iLIF) [31]. (b) Details of the bubble pinch-off process: the center of the meniscus moves inward while the outer region of the meniscus moves outward, leading to the formation of an air cavity that eventually pinches off as an entrained air bubble. The scale bars represent 50 μm.

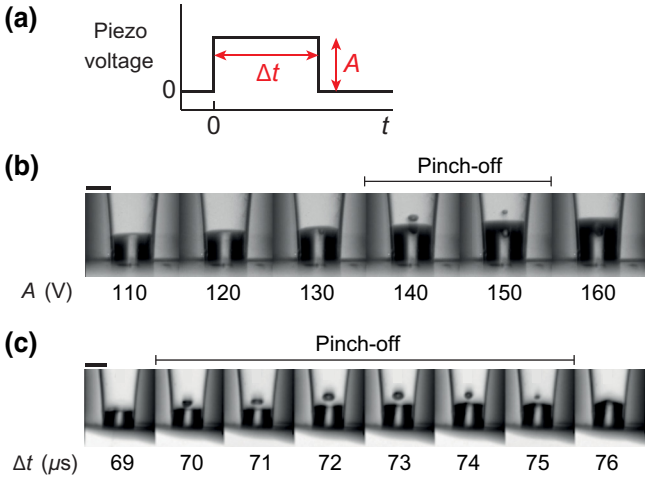

FIG. 2. (a) A rectangular piezo actuation pulse, with its amplitude A and length Δt as the control parameters. (b),(c) The window of bubble pinch-off for (b) a pull-push pulse with a pulse width of 30 μs and a varying amplitude and (c) a pull-push pulse with an amplitude of 94 V and a varying pulse width. The scale bars represent 50 μm.

from the wall to the center of the nozzle [40]. Furthermore, the meniscus can be deformed by geometrical-flow focusing when a pressure wave hits a concave meniscus [41–43]. Finally, meniscus destabilization and the resulting bubble pinch-off can originate from the interaction of capillary waves at the gas-liquid interface. In fact, there is a remarkable similarity between the bubble-entrainment phenomenon in Figs. 1 and 2 and, in particular, the window of bubble entrainment, with bubble pinch-off during crater collapse in drop impact and that during bubble bursting at the surface of a liquid pool [44–49]. In these cases, bubble entrainment is a result of capillary waves traveling down the cavity that then interact at the base of the cavity, leading to the pinch-off of a bubble. Bubble pinch-off has been shown to require perfect timing of capillary-wave interaction and it thereby depends on both the amplitude and the overall shape of the cavity [44,47,49].

The aim of the present study is to find the underlying physical mechanisms that drive bubble pinch-off and entrainment as observed in Figs. 1 and 2 and to gain a fundamental physical insight into the stability of the meniscus in an inkjet nozzle. To that end, after describing the methods for both the experiments and numerics in Sec. II, the meniscus and bubble dynamics shown in Fig. 1 are analyzed in more detail by tracking the meniscus position over time (Sec. III). The driving of the meniscus by the piezo actuator is further characterized by measuring the ring-down piezosignal. Then, the meniscus dynamics of two additional experiments are analyzed to identify the process during which the inner and outer regions of the meniscus develop their destabilizing out-of-phase motion. Finally, the mechanisms that drive the development of this out-of-phase motion are identified using numerical simulations with the boundary-integral (BI) method [42]. The paper ends with conclusions (Sec. IV).

II. EXPERIMENTAL AND NUMERICAL METHODS

A. Printhead and ink

A 70-μm-nozzle-diameter Autodrop Pipette from Microdrop Technologies GmbH (AD-K-501 and AD-H-501) is used [see Fig. 3(a)]. Figure 3(b) shows the approximate inner dimensions of the functional acoustic part of the printhead. More details about this type of printhead can be found in Refs. [50,51].

A 4:1 (v/v) mixture of water with glycerol (Sigma-Aldrich, G9012, 1,2,3-Propanetriol, $\geq$ 99.5%) is used as a model ink. All experiments are performed at room temperature. The density, viscosity, and surface tension σ are taken from the literature to be 1050 kg/m^3, 2.1 mPa s, and 71 mN/m, respectively [52,53]. The model ink is supplied from a plastic syringe to the top of the Autodrop Pipette holder via flexible plastic polyether ether ketone tubing (Upchurch Scientific) and the meniscus is positioned at the nozzle exit by manually adjusting the piston of the syringe.

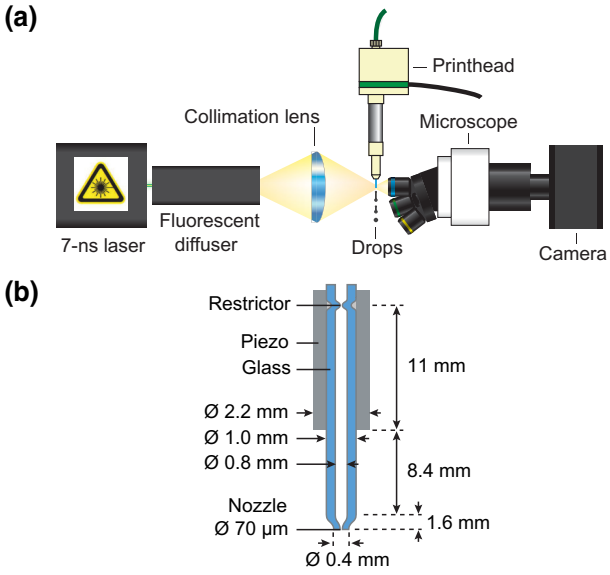

FIG. 3. (a) The experimental setup employed to image meniscus motion and bubble pinch-off in the drop-on-demand piezo-acoustic inkjet nozzle, using illumination by iLIF [31]. (b) A schematic layout of the functional acoustic part of the inkjet printhead. It consists of a glass capillary tube (blue) that is tapered toward the 70-μm-nozzle exit. A cylindrical piezo (gray) can be actuated to drive the ink-channel acoustics and the resulting droplet formation.

B. Imaging setup

Bubble pinch-off is recorded using a stroboscopic imaging setup [see Fig. 3(a)]. The microscope (Olympus) has a 5× objective (LMPLFLN5x, numerical aperture of 0.13), a tube lens (U-TLU), and a high-resolution CCD camera (Lumenera, Lw135m, 1392 × 1040 pixels, 4.65 μm pixel size). The resulting optical resolution is 0.93 μm/pixel. The images captured by the camera are saved using custom-made software on a personal computer (PC) programmed in the graphical programming language LABVIEW (National Instruments).

The tip of the Autodrop Pipette is illuminated by incoherent 8-ns illumination pulses with a wavelength of 577 nm from a laser-induced fluorescence (iLIF) system [31]. The iLIF system consists of a pulsed laser (Quantel Ever-Green, dual cavity Nd:YAG, $\lambda = 532$ nm, 7 ns), a fluorescent plate embedded in a highly efficient diffuser (Lavision, part nos. 1108417 and 1003144), and a lens to condense the light pulses onto the imaging plane of the microscope.

C. Measurement procedure

A programmable pulse-delay generator (Berkeley Nucleonics Corporation, BNC 575) triggers the laser, the camera, and the printhead actuation system with nanosecond precision. The jetting process is kept reproducible by jetting the entrained bubble out after each bubble pinch-off event. To do so, the piezo is actuated by rectangular pulses from two arbitrary waveform generators: one waveform generator (Agilent 33220A, 20 MHz, 14 bit, 50 MS/s) produces one high-amplitude pulse to entrain an air bubble and the other waveform generator (Wavetek 195, 16 MHz, 12 bit, 40 MS/s) successively produces 49 low-amplitude pulses to jet the entrained air bubbles out of the nozzle. The DOD rate is in all cases only 100 droplets/s, such that the ink-channel acoustics are completely damped out and the meniscus position is restored to its equilibrium position before the start of a new actuation pulse. For every actuation cycle, a custom-made LABVIEW program captures one image during the high-amplitude piezo actuation pulse. The timing of the image exposure is controlled by varying the delay of the laser flash with respect to the start of the piezo driving pulse. The delay is varied over a range from 0 μs to 200 μs, with steps of 1 μs, to capture the complete drop formation and bubble pinch-off process. Thus, in total, 200 droplets are imaged out of 10 000 piezo actuations, which demonstrates the extremely high degree of reproducibility of inkjet printing.

A laboratory amplifier (Falco System WMA-300, 5 MHz, 2000 V/μs) amplifies the pulses from the waveform generators by a factor of 50. Given the 5-MHz amplifier bandwidth, the rise-and-fall time of the rectangular pulses is 0.2 μs. Note, however—from, e.g., Fig. 1—that the actual response time of the ink in the nozzle is a little less than 10 μs after applying the driving pulse to the electrical piezo connections at $t = 0$ μs. The rectangular piezo driving pulses have an amplitude between 0 V and 160 V and the printhead can be driven in either the push-pull mode or the pull-push mode by switching the polarity of the electrical connections at the printhead. With the complete system, droplets are produced with diameters in the range of 70–100 μm, corresponding to volumes of 180–520 pl and droplet velocities in the range of 1–3 m s^{-1}.

D. Image analysis

The motion of the meniscus and that of the bubble are tracked as a function of time. First, the contrast in each image is enhanced using ImageJ [54] by subtracting the original image from the image taken at $t = 0$ μs and by adding the inverted result to the original image. Second, the edges of the meniscus and bubble are detected using a script programmed in PYTHON [55]. The script applies a Scikit-Image Canny edge detector to each image, extracts the edges of interest, and calculates their positions. The meniscus is separated into an inner and an outer region to quantify the meniscus shape deformation (see Fig. 4). The inner region is chosen such that it always confines the bubble and has a width of 0.6 times the nozzle diameter. The outer region is set to a width of 0.9 times the nozzle diameter. The position of the outer region of the meniscus y_o is the average position of the detected edge in that region. The position of the inner region of the meniscus y_i is the maximum or minimum position of the detected edge in that region, depending on whether it has a concave or convex shape, respectively. When a bubble is present, its center position y_b and diameter d are determined. The bubble diameter is always measured in the axial direction to minimize a potential error in the bubble diameter due to the refraction of light at the cylindrical walls of the glass nozzle, which can deform the image. However, optical distortion due to refraction is low for three reasons: (i) due

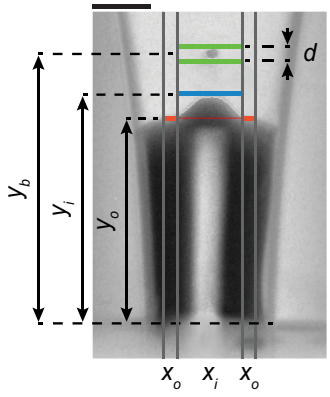

FIG. 4. An example of an image-analysis result, showing the meniscus positions y_o of the outer region x_o and y_i of the inner region x_i, the bubble position y_b, and the bubble diameter d. The scale bar represents 50 μm.

to the similar refractive index of the ink and glass, (ii) because the outer diameter of the glass nozzle (0.4 mm; see Fig. 3) is large compared to the nozzle diameter, and (iii) due to the relatively low numerical aperture of the microscope objective. Consequently, light rays from within the ink in the nozzle region are mostly normal to the glass-air interface upon exiting the glass nozzle toward the microscope objective and, therefore, we do not correct y_o, y_i, and y_b for refraction. The time-dependent positions y_o, y_i, and y_b are filtered to extract the amplitudes and dynamics of the low- and high-frequency components of the meniscus motion.

E. Piezo eigenfrequency characterization through ring-down measurements

To characterize the resonance behavior of the piezo, the ring-down of the piezo is measured using a piezo-sensing technique described in Refs. [2,21]. The piezo is driven using an electrical pulse. Subsequently, when the driving voltage drops below 1 V, the piezo contacts are automatically connected to an oscilloscope that records the ring-down voltage oscillations of the piezo, giving its characteristic resonance frequency.

F. Boundary-integral simulations

To study the bubble pinch-off process and the underlying physical mechanisms in greater detail, BI simulations are performed [42]. The utilized BI code is axisymmetric and assumes irrotational, incompressible, and inviscid flow [56–59]. In essence, the unsteady Bernoulli equation,

$$\frac{\partial \phi}{\partial t} = -\frac{1}{2}|\nabla \phi|^2 - \frac{\Delta p + \kappa \sigma}{\rho}, \tag{1}$$

is time integrated as described in Ref. [42]. In Eq. 1, ϕ is the flow potential, Δp is the pressure variation, κ is the curvature, and σ and ρ are the liquid surface tension and density, respectively. Owing to the micron-sized meniscus, we neglect gravity. The inviscid assumption is appropriate here, as in the experiments it is observed that the meniscus shape deformation is the largest at low viscosity and decreases as the ink viscosity increases. The numerical setup consists of a nozzle wall (solid boundary) and a meniscus (free boundary). The flow in the nozzle is driven by applying a stream-velocity boundary condition to the nodes at the entrance of the nozzle.

Two methods are used sequentially to describe the contact-line dynamics of the meniscus; a fixed contact line and a moving contact line based on contact-angle hysteresis, with a receding contact angle θ_r and an advancing contact angle θ_a. The combination of these two methods provides a good balance between approximating the experimentally observed meniscus motion and preventing numerical instabilities. These occur when the distance between the free boundary and solid boundary becomes too small. At the start of each simulation, the contact line is kept pinned. If, during this first time period, one of the nodes of the meniscus comes within a distance from the wall that will cause numerical instability, the meniscus between that node and the contact line is cut off and a new contact line is created near this node. This intervention does not have a significant effect on the bubble pinch-off phenomena in the simulations. Once the contact angle becomes larger than θ_a, the moving-contact-line method is initiated. This method keeps the contact line pinned for $\theta_r < \theta < \theta_a$; moves the contact line to $\theta = \theta_r$ if $\theta < \theta_r$, and moves the contact line to $\theta = \theta_a$ when $\theta > \theta_a$. θ_r and θ_a are set to the maximum angle away from 90° for which the meniscus motion near the wall remains stable during the simulations, i.e., $\theta_r = 72°$ and $\theta_a = 108°$. At larger angles away from 90°, numerical instabilities will develop on the meniscus because of the too small distance between the free boundary and the solid boundary, as before.

III. RESULTS AND DISCUSSION

A. Meniscus and bubble dynamics

The data shown in Fig. 1 are now analyzed in more detail. Figure 5(a) shows the positions of the outer and inner regions of the meniscus (y_o, y_i) and that of the bubble (y_b) as a function of time. Note that just before pinch-off, a phase difference $\Delta\varphi$ develops between the inner and

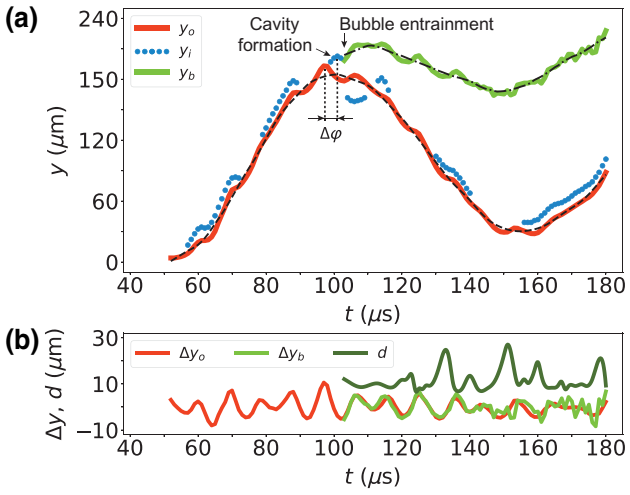

FIG. 5. (a) The meniscus outer, y_o, and inner, y_i, positions and the bubble position, y_b, as functions of time after the start of piezo actuation. The black dashed line and the black dash-dotted line show the low-frequency (low-pass-filtered red curve) motion of the meniscus outer region and that of the bubble (low-pass-filtered green curve), respectively. (b) The high-frequency [high-pass-filtered red curve in (a)] movement of the meniscus outer-region position, Δy_o, and that of the bubble position, Δy_b. The dark green curve shows the bubble diameter d as a function of time.

outer regions of the meniscus, eventually leading to phase inversion. This is the crucial opposing motion between the central cavity and the outer region of the meniscus that leads to bubble pinch-off, as is observed in Fig. 1(b). The process that is responsible for this phase difference is analyzed in Sec. C. Also note in Fig. 5(a) that both the meniscus-position curve and the bubble-position curve have a high-amplitude low-frequency motion of the order of 10 kHz (100-μs period) with, superimposed, a low-amplitude high-frequency motion of the order of 100 kHz (10-μs period). The low-frequency motion of the meniscus and bubble are indicated by the dashed curve and by the dash-dotted curve, respectively.

The high-frequency component in the meniscus motion, Δy_o, and that of the bubble motion, Δy_b, are plotted in Fig. 5(b). In addition, in Fig. 5(b), the bubble diameter d is plotted as a function of time. The bubble equilibrium radius is 5 ± 1 μm, which corresponds to a Minnaert eigenfrequency [60] of approximately 600 kHz. As this is much higher than the observed bubble oscillation frequency of 100 kHz, the radial dynamics of the bubble are considered to oscillate in phase with those of the pressure waves inside the ink channel [61]. Therefore, the bubble radius directly represents the local pressure, i.e., the maximum in the bubble radius corresponds to a minimum pressure and vice versa. Note in Fig. 5(b) that the bubble diameter, the bubble position, and the meniscus position all oscillate at a frequency of 105 ± 5 kHz. Also note that the meniscus and bubble are moving inward around the time that the bubble diameter is a maximum (pressure minimum), while the meniscus and bubble start moving outward when the bubble diameter is a minimum (pressure maximum). Thus, the meniscus and the bubble are driven by the same high-frequency pressure waves and not by their individual eigenmodes.

It may be noted that next to bubble entrainment, Fig. 1 shows another typical inkjet phenomenon called "tail hooking": when the meniscus retracts into the nozzle, the tail sweeps toward a nozzle side to reduce its surface energy [62,63]. Tail hooking typically induces an off-axis jet angle and in Fig. 1 it also results in the deposition of a tiny sessile droplet on the nozzle plate (indicated by the arrow). However, since stroboscopic imaging is used here, i.e., every image shows a different droplet, it can be concluded that the jetting process is highly robust and reproducible. This can also be observed from the absence of any discontinuities in the position and size of the sessile droplet, the bubble, and the jetted droplet.

B. Piezo-actuator characterization

To determine whether the piezo actuator is the origin of the high-frequency pressure oscillations, the eigenmodes of the piezo are characterized by measuring the ring-down signal of the piezo for an empty ink channel. The piezo is first actuated using a pull-push pulse with an amplitude A of 10 V, a full-width-at-half-maximum (FWHM) pulse width Δt of 72 μs, and a rise-and-fall time Δe of 1 μs [see Fig. 6(a)]. The ring-down signal and its Fourier spectrum are plotted in Figs. 6(b) and 6(c). Indeed, in the ring-down signal the same 105-kHz high-frequency component is present as in the meniscus motion, the bubble motion, and the radial dynamics in Fig. 5(b). The piezo eigenmode frequencies are calculated from its dimensions (Fig. 3) and the speed of sound in piezoceramic (approximately 4000 m/s) to be 111 ± 12 kHz in the longitudinal direction and 3.4 ± 0.1 MHz in the radial direction [64,65]. Thus, the 105-kHz high-frequency component in the piezo ring-down signal originates from the longitudinal resonance mode of the piezo and the pressure waves produced by this resonance mode drive the high-frequency motion of the meniscus in the nozzle. Indeed, when the high-frequency component is suppressed by using a Δe of 9 μs [see Figs. 6(b) and 6(c)], the high-frequency motion of the meniscus is also suppressed [see Fig. 6(d)].

Notably, the absence of the 105-kHz high-frequency pressure waves also prevents bubble pinch-off [see Fig. 6(f) in comparison to Fig. 6(e)]. In the experiment shown in Fig. 6(f), an air cavity is still formed but it does not pinch off a bubble. This cavity can be forced to pinch off in the same way as before, but at a different meniscus position and time, by increasing the amplitude of the piezo driving to 120 V [see Fig. 6(g)]. Thus, suppressing the high-frequency pressure waves effectively increases the threshold for bubble pinch-off from 95 V to 120 V. In other words, the high-frequency pressure waves from the longitudinal resonance mode of the piezo promote bubble pinch-off and, through suppression of the 105 kHz waves, the driving amplitude can be increased, allowing for stable inkjet printing at a higher droplet velocity.

C. Meniscus shape deformation process

Now that the driving mechanisms of the meniscus are identified, next, the process responsible for the development of the phase difference between the inner and outer regions of the meniscus, eventually leading to phase inversion and bubble pinch-off, can be identified. The phase difference $\Delta\varphi$ [Fig. 5(a)] develops through the meniscus shape deformation process that can be observed in Fig 7: it develops by jet formation at a concave meniscus. The universality of the meniscus shape deformation process prior to bubble pinch-off is demonstrated in Fig. 7 by its presence in two bubble pinch-off experiments with entirely different driving conditions, namely, with piezo driving pulses with opposite polarity. In the first experiment, the piezo is actuated using a rectangular push-pull pulse ($A = 160$ V, $\Delta t = 30$ μs). A bubble is entrained after droplet formation and it remains inside the nozzle [see Fig. 7(a)]. In the second experiment, the piezo is actuated using a

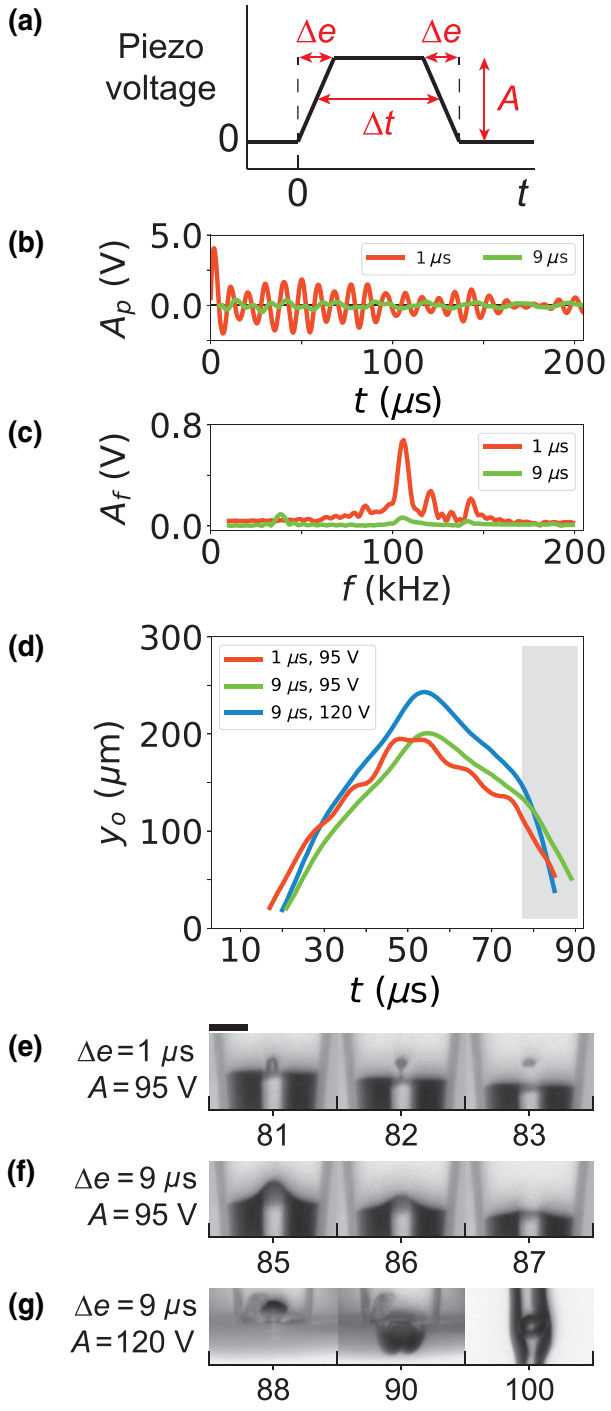

FIG. 6. (a) A piezo actuation pulse with amplitude A, FWHM pulse width Δt, and rise-and-fall time Δe. (b),(c) Piezo (b) ring-down measurements with (c) the corresponding Fourier spectra, for a pull-push pulse with $A = 10$ V, $\Delta t = 72$ μs, and values of Δe as indicated in the legend. (d) The meniscus motion for three pulses with $\Delta t = 72$ μs and with Δe and A as given in the legend. Bubble entrainment takes place in the gray-shaded time window. (e)–(g) Images of the nozzle taken during the time window indicated by the gray-shaded time window in (d), showing whether or not bubble pinch-off takes place. The numbers under the images correspond to the time in μs in (d). The scale bar represents 50 μm.

rectangular pull-push pulse ($A = 150$ V, $\Delta t = 30$ μs). In contrast to the first experiment, a bubble is entrained before droplet formation and it is ejected with the droplet shortly after entrainment [see Fig. 7(b)]. Despite the large differences between the two experiments, the image sequences and graphs in Figs. 7(c)–7(f) show that the meniscus shape deformation process is qualitatively the same for the two experiments. Initially, upon retraction, the meniscus has a concave shape. Then, during the advancing of the meniscus, a small liquid jet is formed in the outward direction. Later, this jet recoils back inward, while the outer region of the meniscus is forced to move outward again, in the opposite direction to the movement of the jet. Similar to the experiment in Fig. 1, the opposing motion of the outer and inner regions of the meniscus leads to the formation and closure of a cavity and thereby to the pinch-off of a bubble. Thus, phase inversion between the inner and outer regions of the meniscus is a consequence of jet formation at the central part of the concave meniscus. The qualitative differences between the meniscus shapes in Figs. 7(c) and 7(d), e.g., the flatter meniscus in (d) as compared to (c), underpin the complex nonlinear behavior of the inkjet nozzle.

D. Jet-formation mechanism

From the literature, it is known that when a pressure wave propels a concave-shaped meniscus forward, a jet forms due to geometrical focusing of the flow at the meniscus due to an inhomogeneous pressure gradient field along the meniscus [42,43]. The pressure gradient and the resulting velocity are larger at the center of a concave meniscus than at its edge (see also Ref. [41]). Thus, in the inkjet nozzle, first, the inward motion of ink results in a concave-shaped meniscus, then a first outward acceleration creates a phase difference between the inner and outer regions of the meniscus by the formation of a central outward-moving liquid jet, and, finally, a well-timed second outward acceleration enhances this phase difference by the formation of a toroidal outward-moving liquid jet. The central liquid jet recoils inward and forms an air cavity that is enclosed by the toroidal outward-moving liquid jet and, as a consequence, a bubble pinches off.

To further demonstrate the details of the proposed pinch-off mechanism, numerical simulations are performed using the BI method. The results are shown in Fig. 8. The geometry of the numerical setup in Fig. 8(a), and the stream-velocity boundary condition $v(t)$ in Fig. 8(b), are chosen such that they follow the experimental conditions, i.e., the nozzle diameter and the 100-kHz oscillations that are identified to drive bubble pinch-off. The initial meniscus shape [Fig. 8(c)] and the imposed amplitude of the 100-kHz velocity boundary condition [Fig. 8(b)] are varied and, as in the experiments, only for highly specific combinations of the two, the meniscus shape deformation process develops toward bubble pinch-off.

In the simulation, we thus start with a retracted concave meniscus with a parabolic and undisturbed profile, as observed in the experiments up to a time of approximately 80 μs in Fig. 1 and 87 μs in Fig. 7. A simulation result is shown in Fig. 8(c). The figure reveals the amplitude and the direction of the ink velocity, and demonstrates how the velocity field inhomogeneity and the focusing of the flow at the concave part of the meniscus drive the jet formation process. Moreover, Fig. 8(c) highlights the opposing motion between the central jet and the toroidal jet and shows in detail how this opposing motion leads to the formation of a cavity that closes and pinches off a bubble. The main steps in this process, which are discussed in detail earlier, are now schematically summarized in Fig. 8(d): a central jet forms at the concave meniscus during the first outward acceleration; then, a toroidal jet forms at the concave meniscus around the central jet during the second outward acceleration; and, finally, the recoiling central jet forms a cavity and the progressing toroidal jet encloses this cavity, with bubble pinch-off as a result.

Note that even though the BI simulations are incompressible, we observe the same meniscus deformation process as in the experiments, suggesting that the meniscus shape deformation process responsible for bubble pinch-off does not require acoustics but that a certain unbalance between the capillary and inertial time scales is sufficient. Indeed, the capillary time scale ($\tau_c = \sqrt{\rho R^3/\sigma}$, with R the nozzle radius) for the present inkjet nozzle is approximately 24 μs, whereas the inertial time scale is of the order of 1 μs, i.e., set by the rise-and-fall time of $v(t)$ in Fig. 8(b). Furthermore, from the input velocity boundary condition $v(t)$ and Eq. (1), the dynamic driving pressure in the BI simulations can be calculated, as follows: $\Delta p = \Delta p_a + \Delta p_i = -\rho(\partial\phi/\partial t) - (1/2)\rho U^2$, where Δp_a and Δp_i are the pressure contributions from acceleration and inertia, respectively. The magnitude of Δp_i is directly estimated from $v(t)$ as 8 kPa. The magnitude of Δp_a can be estimated as $\rho UL/\Delta t \approx 1.4$–12 bar, where U is the velocity variation (4 m/s) over time Δt [1 μs; see Fig. 8(b)] and L is a length scale between the nozzle radius (35 μm) and the fluid-filled domain [300 μm; see Fig. 8(a)]. Note that since the BI simulations are incompressible, these dynamic pressure fluctuations are to be compared with acoustic pressure fluctuations in the experiment. The order of magnitude of the dynamic driving pressure amplitude is in line with values reported for the acoustic driving pressure in inkjet printing [2,30], which once more shows that acoustic wave propagation is not required for the observed bubble pinch-off phenomenon and that it is a flow-dominated process.

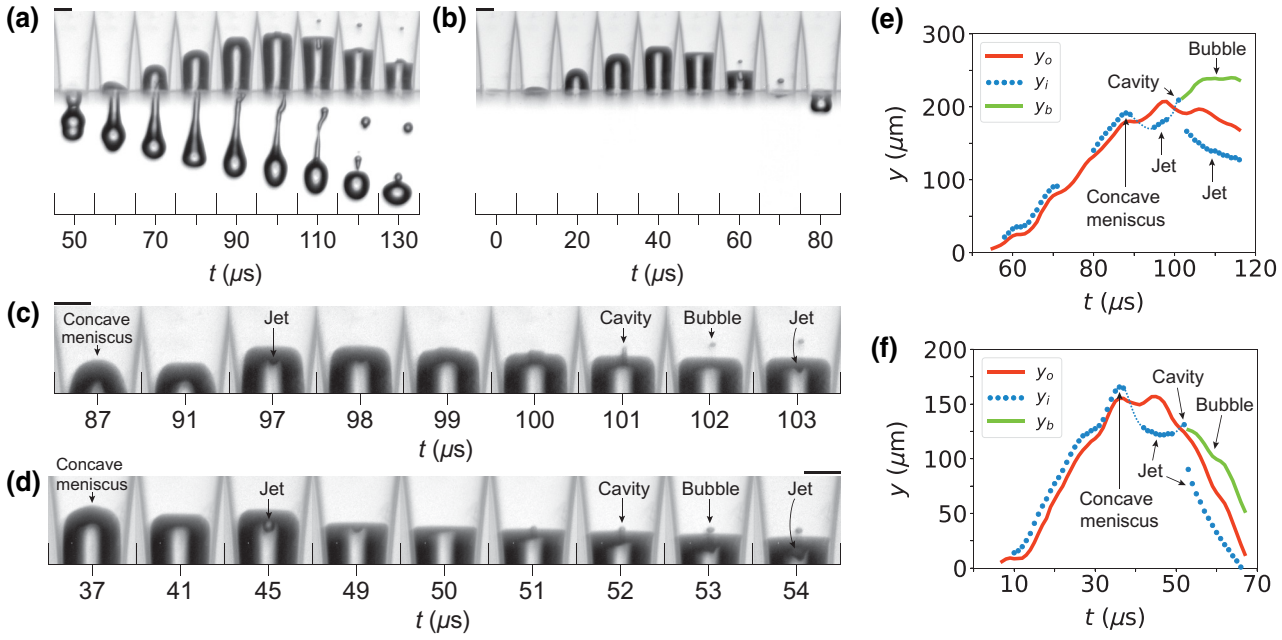

FIG. 7. Bubble pinch-off for (a) a rectangular push-pull pulse with an amplitude of 160 V and a width of 30 μs and (b) a rectangular pull-push pulse with an amplitude of 150 V and a width of 30 μs. (c),(d) Details of the meniscus shape deformation process prior to, during, and after bubble pinch-off for the push-pull and the pull-push pulse, respectively. (e),(f) The meniscus outer-region position y_o, inner-region position y_i, and bubble position y_b as a function of time for the push-pull and pull-push pulse, respectively. The thin blue dashed line is added to guide the eye in the parts of the jet-formation and jet-recoil process where the position of the inner region of the meniscus cannot be tracked. The scale bars represent 50 μm.

E. The bubble pinch-off window

Using the knowledge acquired on the underlying physics of the bubble pinch-off phenomenon studied in this work, we now qualitatively explain the observed parameter windows of bubble pinch-off in Fig. 2. In Fig. 2(b), the pulse width Δt is fixed and the amplitude A is varied. At an amplitude of 130 V and lower, the velocity difference between the recoiling central jet and the progressing toroidal jet is not high enough to form a sufficiently deep cavity at the right moment in time and to enclose this cavity. At an amplitude of 160 V, the central jet has such a length and inertia that it is too slow to recoil before the toroidal jet reaches the central axis. As a result, the toroidal jet encloses the base of the central jet, which in multiple experiments and simulations has been observed to result in the formation of a toroidal bubble such as shown experimentally in Fig. 9(a) and from a BI simulation in Fig. 9(b).

In Fig. 2(c), the amplitude A is fixed and the pulse width Δt is varied. In other words, the control parameter in these experiments is the timing of the outward acceleration of the meniscus by the falling edge of the piezo driving pulse. In the experiments shown in Fig. 2(c), the central jet has already been formed before the falling edge of the pulse. At the different times of meniscus acceleration, the meniscus shape is different and thus the toroidal jet-formation process is different. At $\Delta t = 69$ μs, the acceleration is too early, i.e., the central jet is not able to develop sufficient opposing motion with respect to the toroidal jet because of its early formation. At $\Delta t = 76$ μs, the acceleration is too late, i.e., the meniscus is propelled outward while the cavity is already present; thus, the central cavity

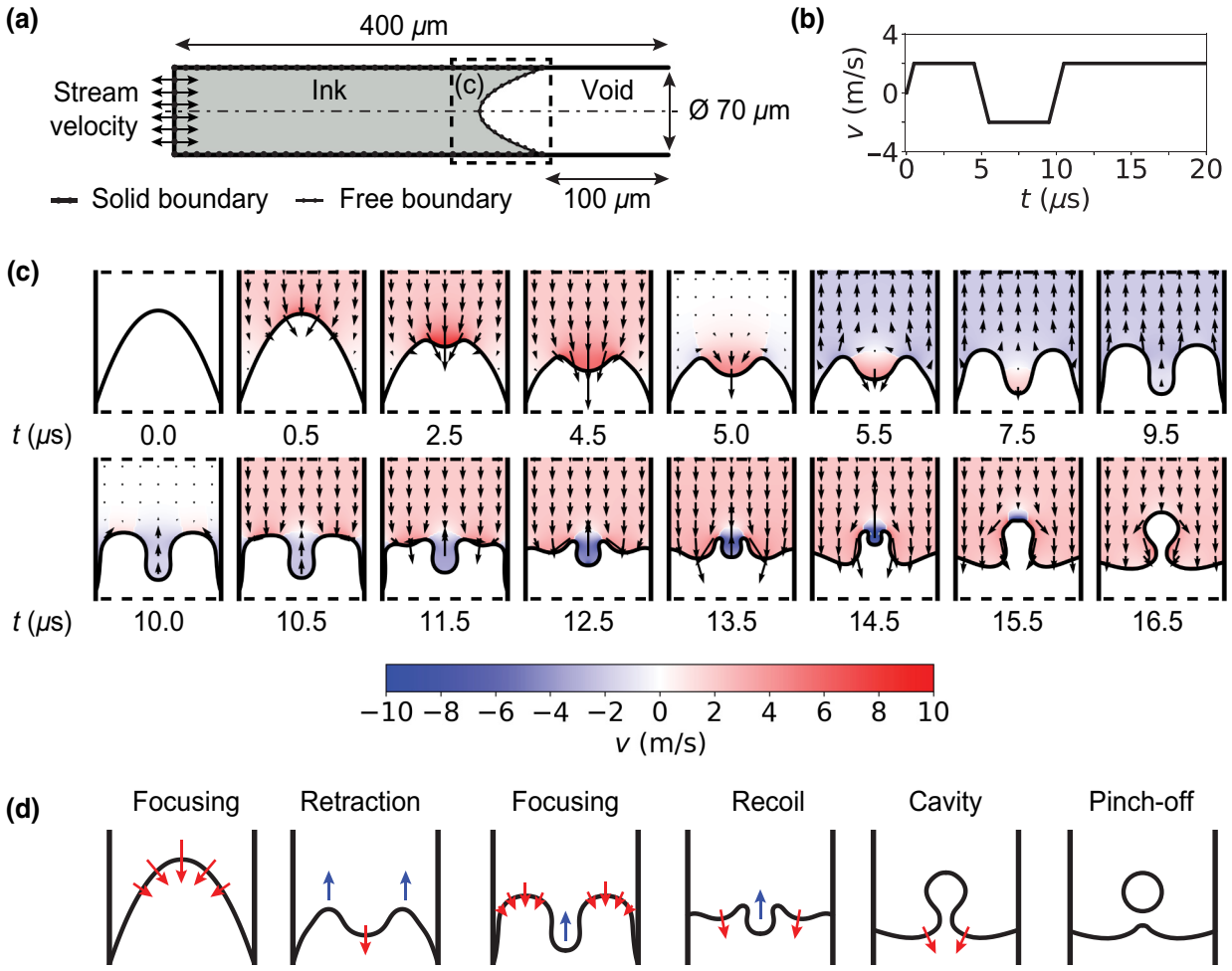

FIG. 8. (a) The numerical setup for the BI simulation, where the left boundary is subject to a stream-velocity boundary condition. The initial meniscus shape is a parabola with a depth of 0.75 times the nozzle diameter. (b) The stream-velocity boundary condition v for the numerical setup as a function of time with a 100-kHz velocity oscillation followed by an outward-directed flow. (c) The meniscus shape deformation process prior to bubble pinch-off, simulated using the BI method. (d) A schematic summary of the main steps in (c).

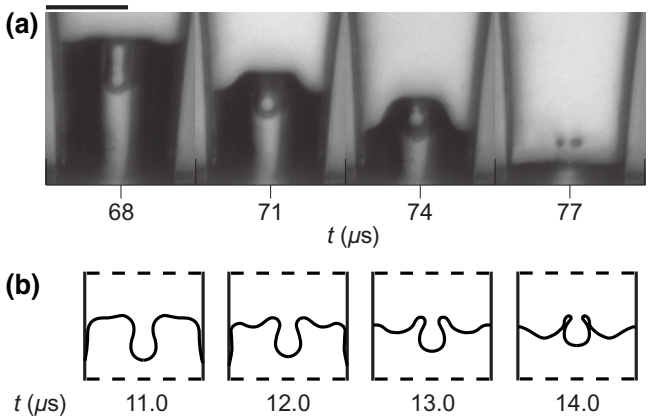

FIG. 9. (a) Toroidal bubble pinch-off as experimentally recorded for a rectangular pull-push pulse with an amplitude of 92 V and a width of 53 μs. The scale bar represents 50 μm. (b) A simulation using the BI method of the meniscus shape deformation process eventually leading to toroidal bubble pinch-off.

is propelled outward faster than the outer region of the meniscus.

Despite the acquired knowledge on the underlying physics of the bubble pinch-off mechanism, it remains difficult to predict where exactly in the piezo driving parameter space bubble pinch-off will occur, as is also the case for bubble pinch-off after drop impact on a liquid pool [44,47]. The two main reasons are the sensitivity of the mechanism to the operating conditions and the unavailability of information about the exact printhead configuration and its detailed acoustic properties. However, also in printheads with different dimensions and thus different driving acoustics, the authors have observed highly similar meniscus deformation and pinch-off processes. As a practical guideline, bubble pinch-off can be suppressed with relative ease by suppressing the high-frequency component in the acoustics through the edge duration of the piezo driving pulse. Another simple method, which is not studied here, is to damp out the meniscus shape deformations by increasing the ink viscosity. However, this requires higher driving amplitudes to produce droplets at equal velocity and reduces the universal applicability of the technique. The role of ink viscosity on meniscus deformations due to flow focusing in an inkjet nozzle will be part of future work, as well as remaining questions as to the physics that dictates the size of the entrained bubble.

IV. CONCLUSIONS

An oscillating meniscus in a piezo-inkjet nozzle can pinch off a bubble in a specific window of driving conditions, thereby excluding the Rayleigh-Taylor instability as the primary driving mechanism. Pinch-off is the result of the closure of a central air cavity in the meniscus that forms due to opposing motion between a central region and an outer region of the meniscus. The opposing motion between the central region and outer region of the meniscus is the result of jet formation at the concave meniscus. We reveal that jet formation is driven by flow focusing, i.e., due to the inhomogeneous pressure gradient field along the meniscus, as confirmed by the BI simulations. The process that is responsible for the bubble pinch-off can be summarized as follows. The meniscus gains a concave shape due to inward motion. Subsequently, a first outward acceleration produces a central jet at the concave meniscus. A well-timed second outward acceleration produces a toroidal jet at the concave meniscus around the central jet. The recoiling central jet forms a central air cavity while the progressing toroidal jet encloses this air cavity. Eventually, this leads to pinch-off of an air bubble. These results contribute to a fundamental understanding of the stability of the oscillating meniscus in an inkjet printhead and thereby provide ways to increase the stability of inkjet printing, such as the suppression of higher harmonics of the fundamental resonance mode of the ink channel by changing the piezo driving pulse rather than the nozzle or piezo design. The results from the incompressible BI simulations suggest that bubble pinch-off requires a certain unbalance between the capillary and inertial time scales and that it is therefore a flow-driven phenomenon that does not require acoustics. Future work will focus on further elucidating the role of liquid viscosity and meniscus velocity on bubble pinch-off and entrainment.

ACKNOWLEDGMENTS

This work is part of the research program "High Tech Systems and Materials" (HTSM), with project number 12802, and part of the Industrial Partnership Programme, number i43, of the Dutch Technology Foundation (STW) and the Foundation for Fundamental Research on Matter (FOM), which are part of the Netherlands Organisation for Scientific Research (NWO). The research was cofinanced by Canon Production Printing Netherlands B.V., the University of Twente, and Eindhoven University of Technology.

[1] O. A. Basaran, Small-scale free surface flows with breakup: Drop formation and emerging applications, AIChE J. **48**, 1842 (2002).
[2] H. Wijshoff, The dynamics of the piezo inkjet printhead operation, Phys. Rep. **491**, 77 (2010).
[3] S. D. Hoath, *Fundamentals of Inkjet Printing: The Science of Inkjet and Droplets* (Wiley-VCH Verlag GmbH & Co. KGaA, Hoboken, New Jersey, USA, 2015).
[4] D. Lohse, Fundamental fluid dynamics challenges in inkjet printing, Annual Review of Fluid Mechanics (to be published 2021).

[5] A. Fraters, R. Jeurissen, M. van den Berg, H. Reinten, H. Wijshoff, D. Lohse, M. Versluis, and T. Segers, Secondary Tail Formation and Breakup in Piezoacoustic Inkjet Printing: Femtoliter Droplets Captured in Flight, Phys. Rev. Appl. **13**, 024075 (2020).

[6] S. Majee, M. Song, S.-L. Zhang, and Z.-B. Zhang, Scalable inkjet printing of shear-exfoliated graphene transparent conductive films, Carbon **102**, 51 (2016).

[7] S. Majee, C. Liu, B. Wu, S.-L. Zhang, and Z.-B. Zhang, Ink-jet printed highly conductive pristine graphene patterns achieved with water-based ink and aqueous doping processing, Carbon **114**, 77 (2017).

[8] S. K. Eshkalak, A. Cinnappan, W. A. D. M. Jayathilaka, M. Khatibzadeh, E. Kowsari, and S. Ramakrishna, A review on inkjet printing of CNT composites for smart applications, Appl. Mater. Today **9**, 372 (2017).

[9] M. Vilardell, X. Granados, S. Ricart, I. Van Driessche, A. Palau, T. Puig, and X. Obradors, Flexible manufacturing of functional ceramic coatings by inkjet printing, Thin Solid Films **548**, 489 (2013).

[10] A. Moya, G. Gabriel, R. Villa, and F. J. del Campo, Inkjet-printed electrochemical sensors, Curr. Opin. Electrochem. **3**, 29 (2017).

[11] T. M. Eggenhuisen, Y. Galagan, E. W. C. Coenen, W. P. Voorthuijzen, M. W. L Slaats, S. A. Kommeren, S. Shanmuganam, M. J. J. Coenen, R. Andriessen, and W. A. Groen, Digital fabrication of organic solar cells by inkjet printing using non-halogenated solvents, Solar Energy Mater. Solar Cells **134**, 364 (2015).

[12] S. G. Hashmi, M. Ozkan, J. Halme, K. D. Misic, S. M. Zakeeruddin, J. Paltakari, M. Grätzel, and P. D. Lund, High performance dye-sensitized solar cells with inkjet printed ionic liquid electrolyte, Nano Energy **17**, 206 (2015).

[13] T. Shimoda, K. Morii, S. Seki, and H. Kiguchi, Inkjet printing of light-emitting polymer displays, Inkjet Printing Funct. Mater. **28**, 821 (2003).

[14] C. Jiang, L. Mu, J. Zou, Z. He, Z. Zhong, L. Wang, M. Xu, J. Wang, J. Peng, and Y. Cao, Full-color quantum dots active matrix display fabricated by ink-jet printing, Sci. China Chem. **60**, 1349 (2017).

[15] R. Daly, T. S. Harrington, G. D. Martin, and I. M. Hutchings, Inkjet printing for pharmaceutics—a review of research and manufacturing, Int. J. Pharmaceutics **494**, 554 (2015).

[16] A. Simaite, F. Mesnilgrente, B. Tondu, P. Souères, and C. Bergaud, Towards inkjet printable conducting polymer artifical muscles, Sens. Actuators B: Chem. **229**, 425 (2016).

[17] S. Hewes, A. D. Wong, and P. C. Searson, Bioprinting microvessels using and inkjet printer, Bioprinting **7**, 14 (2017).

[18] M. Nakamura, A. Kobayashi, F. Takagi, A. Watanabe, Y. Hiruma, K. Ohuchi, Y. Iwasaki, M. Horie, I. Morita, and S. Takatani, Biocompatible inkjet printing technique for designed seeding of individual living cells, Tissue. Eng. **11**, 1658 (2005).

[19] G. Villar, A. D. Graham, and H. Bayley, A tissue-like printed material, Science **340**, 48 (2013).

[20] W. M. van der Kruk, S. A. Smit, T. J. Segers, X. M. Li, and Ch. Venner, Drop-on-demand printing as novel method of oil supply in elastohydrodynamic lubrication, Tribology Lett. **67**, 1 (2019).

[21] J. de Jong, G. de Bruin, H. Reinten, M. van den Berg, H. Wijshoff, M. Versluis, and D. Lohse, Air entrapment in piezo-driven inkjet printheads, J. Acoust. Soc. Am. **120**, 1257 (2006).

[22] J. de Jong, R. Jeurissen, H. Borel, M. van den Berg, H. Wijshoff, H. Reinten, M. Versluis, A. Prosperetti, and D. Lohse, Entrapped air bubbles in piezo-driven inkjet printing: Their effect on the droplet velocity, Phys. Fluids **18**, 121511 (2006).

[23] R. Jeurissen, J. de Jong, H. Reinten, M. van den Berg, H. Wijshoff, M. Versluis, and D. Lohse, Effect of an entrained air bubble on the acoustics of an ink channel, J. Acoust. Soc. Am. **123**, 2496 (2008).

[24] R. Jeurissen, A. van der Bos, H. Reinten, M. van den Berg, H. Wijshoff, J. de Jong, M. Versluis, and D. Lohse, Acoustic measurement of bubble size in an inkjet printhead, J. Acoust. Soc. Am. **126**, 2184 (2009).

[25] S. J. Lee, D. H. Kwon, and Y. S. Choi, Dynamics of entrained air bubbles inside a piezodriven inkjet printhead, Appl. Phys. Lett. **95**, 221902 (2009).

[26] B.-H. Kim, T.-G. Kim, T.-K. Lee, S. Kim, S.-J. Shin, S.-J. Kim, and S.-J. Lee, Effects of trapped air bubbles on frequency responses of the piezo-driven inkjet printheads and visualization of the bubbles using synchrotron X-ray, Sens. Actuators A: Phys. **154**, 132 (2009).

[27] R. Jeurissen, H. Wijshoff, M. van den Berg, H. Reinten, and D. Lohse, Regimes of bubble volume oscillations in a pipe, J. Acoust. Soc. Am. **130**, 3220 (2011).

[28] A. van der Bos, T. Segers, R. Jeurissen, M. van den Berg, H. Reinten, H. Wijshoff, M. Versluis, and D. Lohse, Infrared imaging and acoustic sizing of a bubble inside a micro-electro-mechanical system piezo ink channel, J. Appl. Phys. **110**, 034503 (2011).

[29] A. Fraters, T. Segers, M. van den Berg, H. Reinten, H. Wijshoff, D. Lohse, and M. Versluis, Shortwave infrared imaging setup to study entrained air bubble dynamics in a mems-based piezo-acoustic inkjet printhead, Exp. Fluids **60**, 123 (2019).

[30] A. Fraters, M. van den Berg, Y. de Loore, H. Reinten, H. Wijshoff, D. Lohse, M. Versluis, and T. Segers, Inkjet Nozzle Failure by Heterogeneous Nucleation: Bubble Entrainment, Cavitation, and Diffusive Growth, Phys. Rev. Appl. **12**, 064019 (2019).

[31] J. A. van der Bos, A. G. Zijlstra, E. C. Gelderblom, and M. Versluis, iLIF: Illumination by laser-induced fluorescence for single flash imaging on a nanoseconds timescale, Exp. Fluids **51**, 1283 (2011).

[32] M. Versluis, High-speed imaging in fluids, Exp. Fluids **54**, 1 (2013).

[33] C. S. Ravasio, S. D. Hoath, G. D. Martin, P. Boltryk, and M. Dorrestijn, in *NIP & Digital Fabrication Conference* (Society for Imaging Science and Technology, 2016), Vol. 2016, p. 348.

[34] H. C. Nallan, J. A. Sadie, R. Kitsomboonloha, S. K. Volkman, and V. Subramanian, Systematic design of jettable

nanoparticle-based inkjet inks: Rheology, acoustics, and jettability, Langmuir **30**, 13470 (2014).
[35] Rayleigh, Investigation of the character of the equilibrium of an incompressible heavy fluid of variable density, Proc. London Math. Soc. **14**, 170 (1883).
[36] G. Taylor, The instability of liquid surfaces when accelerated in a direction perpendicular to their planes. i, Proc. R. Soc. London A **201**, 192 (1950).
[37] M. Faraday, On a peculiar class of acoustical figures; and on certain forms assumed by groups of particles upon vibrating elastic surfaces, Philos. Trans. R. Soc. London **121**, 299 (1831).
[38] M.-J. van der Meulen, H. Reinten, H. Wijshoff, M. Versluis, D. Lohse, and P. Steen, Non-Axisymmetric Effects in Drop-On-Demand Piezo-Acoustic Inkjet Printing, Phys. Rev. Appl. **13**, 054071 (2020).
[39] D. A. Tence, S. S. Berger, and R. F. Burr, Method and apparatus for producing dot size modulation ink jet printing, U.S. Patent 5689291, November 2007.
[40] A. U. Chen and O. A. Basaran, A new method for significantly reducing drop radius without reducing nozzle radius in drop-on-demand drop production, Phys. Fluids **14**, L1 (2002).
[41] A. Antkowiak, N. Bremond, S. Le Dizès, and E. Villermaux, Short-term dynamics of a density interface following an impact, J. Fluid Mech. **577**, 241 (2007).
[42] I. R. Peters, Y. Tagawa, N. Oudalov, C. Sun, A. Prosperetti, D. Lohse, and D. van der Meer, Highly focused supersonic microjets: Numerical simulations, J. Fluid Mech. **719**, 587 (2013).
[43] J. M. Gordillo, H. Onuki, and Y. Tagawa, Impulsive generation of jets by flow focusing, J. Fluid Mech. **894**, A3 (2020).
[44] H. N. Oguz and A. Prosperetti, Bubble entrainment by the impact of drops on liquid surfaces, J. Fluid Mech. **219**, 143 (1990).
[45] H. C. Pumphrey and P. A. Elmore, The entrainment of bubbles by drop impacts, J. Fluid Mech. **220**, 539 (1990).
[46] S. T. Thoroddsen, K. Takehara, H. D. Nguyen, and T. G. Etoh, Singular jets during the collapse of drop-impact craters, J. Fluid Mech. **848**, R3 (2018).
[47] P. Sleutel, P.-H. Tsai, S. Wildeman, W. Bouwhuis, M.-J. Thoraval, C.-W. Visser, A.-B. Wang, M. Versluis, and D. Lohse, Bubble entrainment at high-speed microdroplet impact on a liquid pool, Journal of Fluid Mechanics (to be published).
[48] L. Duchemin, S. Popinet, C. Josserand, and S. Zaleski, Jet formation in bubbles bursting at a free surface, Phys. Fluids **14**, 3000 (2002).
[49] J. M. Gordillo and J. Rodríguez-Rodríguez, Capillary waves control the ejection of bubble bursting jets, J. Fluid Mech. **867**, 556 (2019).
[50] J. F. Dijksman, Hydrodynamics of small tubular pumps, J. Fluid Mech. **139**, 173 (1984).
[51] J. F. Dijksman, Hydro-acoustics of piezoelectrically driven ink-jet print heads, Flow, Turbulence Combustion **61**, 211 (1998).
[52] J. B. Segur and H. E. Oberstar, Viscosity of glycerol and its aqueous solutions, Ind. Eng. Chem. **43**, 2117 (1951).
[53] Glycerine Producers' Association, *Physical properties of glycerine and its solutions* (1963).
[54] ImageJ, http://imagej.nih.gov/ij.
[55] Python Software Foundation, Fredericksburg, Virginia, USA, https://www.python.org/.
[56] H. N. Oğuz and A. Prosperetti, Dynamics of bubble growth and detachment from a needle, J. Fluid Mech. **257**, 111 (1993).
[57] H. Power and L. C. Wrobel, *Boundary Integral Methods in Fluid Mechanics* (Computational Mechanics Publications, 1995).
[58] R. Bergmann, D. van der Meer, S. Gekle, A. van der Bos, and D. Lohse, Controlled impact of a disk on a water surface: Cavity dynamics, J. Fluid Mech. **633**, 381 (2009).
[59] S. Gekle, J. M. Gordillo, D. van der Meer, and D. Lohse, High-Speed Jet Formation after Solid Object Impact, Phys. Rev. Lett. **102**, 034502 (2009).
[60] M. Minnaert, XVI, On musical air-bubbles and the sounds of running water, London, Edinburgh, Dublin Philos. Mag. J. Sci. **16**, 235 (1933).
[61] T. G. Leighton, *The Acoustic Bubble* (Academic Press, London, UK, 1994).
[62] J. Castrejón-Pita, G. Martin, and I. Hutchings, Experimental study of the influence of nozzle defects on drop-on-demand ink jets, J. Imaging Sci. Technol. **55**, 40305 (2011).
[63] M.-J. Van Der Meulen, H. Reinten, H. Wijshoff, M. Versluis, D. Lohse, and P. Steen, Nonaxisymmetric Effects in Drop-On-Demand Piezoacoustic Inkjet Printing, Phys. Rev. Appl. **13**, 054071 (2020).
[64] APC International, Ltd., *Piezoelectric Ceramics: Principles and Applications* (APC International, 2011).
[65] APC International, Ltd., APC Piezo Calculator, https://www.americanpiezo.com/knowledge-center/apc-piezo-calc.html.

Correction: The previously published Figure 6 contained incomplete images in parts (e) and (g) and has been replaced.